JOURNAL OF OPTOELECTRONICS AND ADVANCED MATERIALS Vol. 9, No. 5, May 2007, p. 1555 - 1560

Crystalline and electronic structure of gold nanoclusters determined by EXAFS, XRD and XPS methods

N. ALDEA[a*], P. MARGINEAN[a], V. REDNIC[a], S. PINTEA[a], B. BARZ[b], A. GLUHOI[c], B. E. NIEUWENHUYS[c], XIE YANING[d], F ALDEA[e], M. NEUMANN[f]

[a]*National Institute for Research and Development of Isotopic and Molecular Technologies, Romania*
[b]*University of Missouri-Columbia, 223 Phys Building MO 65211*
[c]*Leiden Institute of Chemistry, Leiden University, The Netherlands*
[d]*Beijing Synchrotron Radiation Facilities of Beijing Electron Positron Collider, Coordination Laboratory of National Center for Nanoscience and Nanotechnology, Beijing, People's Republic of China*
[e] *University of Agriculture Sciences and Veterinary Medicine, Math. Department. Cluj-Napoca, Romania*
[f] *University of Osnabrück, Fachbereich Physik, 49069 Osnabrück, Germany*

Gold particles nanoclusters as supported catalysts were analyzed by extended X-ray absorption fine structure, X-ray diffraction and X-ray photoelectron spectroscopy in order to determine their local, global and electronic structure. The present study points out the strong deformation of the local structure of the active metal due to its interaction with oxide supports as well as a possible oxidation state of the gold component. The average particle size and the microstrain parameters of the supported Au nanoclusters were determined by X-ray diffraction method, based on the Fourier transform of the experimental X-ray line profiles. The global structure is obtained with a fitting method using of the generalized Fermi function facilities for the approximation technique. The strong interaction between the metal nanoclusters and oxide supports induces a great change in the local and global microstructures of the catalysts, modifying at the same time the chemisorptions and catalytic processes that occur at the Au-support interface. The following catalyst samples were investigated: $Au/ZnO/MgO/Al_2O_3$, $Au/CuO/Al_2O_3$ and $Au/Li_2O/CeO_2/Al_2O_3$. The XPS technique was used for determining the electronic states of gold, gold oxide and metal oxides in the oxide supports.

(Received November 14, 2006; accepted April 12, 2007)

Keywords: Supported gold catalysts, X-ray diffraction, X-ray absorption spectroscopy, X-ray photoelectron spectroscopy, Metal support interaction, Local and global structure

1. Introduction

A short theoretical background of the extended X-ray absorption fine structure (EXAFS) and the X-ray diffraction (XRD) analyses, including the main mathematical properties of the generalized Fermi function (GFF), used for approximation and deconvolution of the experimental X-ray line profiles (XRLP) are presented in sections one and three of the paper [1-3]. The fluorescence EXAFS measurements on L_{III} gold edge were carried out in 4W1B beam lines operating at 30-50 mA and 2.2 GeV with an energy resolution of 0.5-3 eV at 10 KeV, at room temperature [4]. The X-ray (111), (200), (220) and (311) diffraction data for supported gold catalysts were collected using a Rigaku rotating anode setup, in Bragg-Brentano geometry with Ni filtered Cu K_α radiation, λ=1.5406 Å at room temperature. A NaI (Tl) detector was used and the signals were amplified and fed to a single channel analyzer (ORTEC 850) read out by a computer.

The XPS spectra were recorded using a PHI 5600ci ESCA spectrometer with monochromatic Al K_α X-ray radiation (1486.6 eV) at room temperature. The pressure in the ultra-high vacuum chamber was within the 10^{-10} mbar range during the measurements. The neutralizer was used in every case due to a charge effect which occurs for nonconducting samples. The binding energy was determined by reference to the C 1s line at 284.8 eV.

Supported gold catalysts were prepared by homogeneous deposition-precipitation with urea on support of MO_x/Al_2O_3 (M: Cu, Ce, Mg, Li in different combinations). The gold precursor was $HAuCl_4 \cdot 3H_2O$, Aldrich, 99.999% purity [5]. The theoretical gold content for the catalysts was 5 wt %. The catalysts were calcined at 300 ^oC before the measurements.

2. EXAFS analysis

The interference between the outgoing and backscattered electron waves has the effect of modulating the X-ray absorption coefficient. The EXAFS function $\chi(k)$ is defined in terms of the atomic absorption coefficient by,

$$\chi(x) = \frac{\mu(k) - \mu_0(k)}{\mu_0(k)} \quad (1)$$

The theoretical EXAFS signal is defined by the relation

$$\chi(k) = \sum_j A_j(k) \sin[2kr_j + \delta_j(k)], \qquad (2)$$

where

$A_j(k) = \left(\frac{N_j}{kr_j^2}\right) F(k,r,\pi) \exp[-2r_j / \lambda(k)] \exp(-2k^2\sigma_j^2)$, r_j - the radial distance, N_j – the number of atoms in the j[th] shell, $\delta_j(k)$ - the phase shift function, σ_j - the root mean square deviation of the distance about r_j, $F(k, r, \pi)$ - the backscattering and $\lambda_j(k)$ - the mean free path function for inelastic scattering. The single shell contribution may be isolated by Fourier transform technique

$$\Phi(r) = (1/2\pi)^{1/2} \int_{k_{\min}}^{k_{\max}} k^n \chi(k) \exp(-2ikr) WF(k) dk, \qquad (3)$$

where $WF(k)$ is the window function used for the minimization of the spurious errors. The inverse Fourier transform of the radial structure function is obtained for any coordination shell with:

$$\chi_j(k) = (2/\pi)^{1/2} (1/k^n) WF(k) \int_{R_{1j}}^{R_{2j}} \Phi_n(r) \exp(2ikr) dr. \qquad (4)$$

The structural parameters for each coordination shell are determined by fitting the experimental spectrum with the theoretical function [1,2].

3. X-ray diffraction analysis

The global structure is obtained with a new fitting method based on the GFF facilities for approximation and the Fourier transform of the experimental XRLP and the instrumental function. The GFF is a simple function with a minimal number of parameters, suitable for XRLP global approximation, based on minimization methods [1] and it is defined by the relation

$$h(s) = \frac{A}{e^{-a(s-c)} + e^{b(s-c)}} \qquad (5)$$

where A, a, b, c are unknown parameters and $s = 2\sin(\theta)/\lambda$. The values A and c describe the amplitude and the position of the XRLP while a and b control its shape.

The integral width of the GFF distribution and the module of the Fourier transform for the true sample were determined by the deconvolution technique and they have the following forms

$$\delta(a,b) = \frac{\pi}{\left(a^a b^b\right)^{1/(a+b)} \cos\left(\frac{\pi}{2}\frac{a-b}{a+b}\right)} \qquad (6)$$

$$|F(L)| = \frac{A_h \rho_g}{A_g \rho_h} \sqrt{\frac{\cos^2\alpha + \sinh^2\beta L}{\cos^2\gamma + \sinh^2\delta L}} \qquad (7)$$

where $\rho = \frac{a+b}{2}$, $q = \frac{a-b}{2}$, $\alpha = \frac{\pi q_g}{2\rho_g}$, $\beta = \frac{\pi^2}{\rho_g}$, $\gamma = \frac{\pi q_h}{2\rho_h}$ and $\delta = \frac{\pi^2}{\rho_h}$

The true sample XRLP and its integral width are given by the relations:

$$f(s^*) = \frac{2A_h\rho_g}{\pi A_g} \frac{\cos\frac{\pi\rho_h}{2\rho_g}\cosh\rho_h s^*}{\cos\frac{\pi\rho_h}{2\rho_g} + \cosh\rho_h s^*} \qquad (8)$$

$$\delta(\rho_h, \rho_g) = \frac{\pi}{2\rho_h \cos\frac{\pi\rho_h}{2\rho_g}} \left(\cos\frac{\pi\rho_h}{\rho_g} + 1\right) \qquad (9)$$

where the indices h, g refer to the experimental and the instrumental profiles. Based on Warren and Averbach theory, the general form of the Fourier transform of the true sample for cubic lattices is obtained from the general relation [3],

$$F(L) = e^{-\left(\frac{|L|}{D_{eff}(hkl)} + \frac{2\pi^2\langle\varepsilon_L^2\rangle_{hkl} h_0^2 L^2}{a^2}\right)} \qquad (10)$$

where $D_{eff}(hkl)$ is the effective crystallite size, $\langle\varepsilon^2\rangle_{hkl}$ is the microstrain of the lattice and $h_0^2 = h^2 + k^2 + l^2$. The data processing of the XRLP presented in the third section is based on the GFF approximation and on its remarkable properties. The effective crystallite size, $D_{eff}(hkl)$ and the microstrain of the lattice $\langle\varepsilon^2\rangle_{hkl}$ were calculated using Eqs. (5-10). Our computer package program SIZE, written in Maple language, has implemented all the procedures for the global structure determination of the nanostrucured materials by data processing of the XRLP.

4. XPS analysis

X-ray photoelectron spectroscopy is widely used in catalysis because it allows determination of the chemical state of the elements of solid surface such as oxidation number and the electronic interactions with neighboring elements from the first coordination shells. In the case of reducible metals the XPS information are very complementary to those of the temperature programmed reduction (TPR). SimPeak computer package program was used for data analysis of the XPS spectra. They are global approximated by the asymmetric Donjac-Sunjic distribution using Levenberg Marquardt algorithm. For background correction we used Tougaard algorithm based on mathematical description of the electron transport.

5. Results and discussion

5.1. EXAFS results

In Figs. 1-3 the numbers (0), (2), (3) and (10) represent the spectra of gold foil used as instrumental correction in the XRD analysis for Au/ $ZnO/MgO/Al_2O_3$, Au/ CuO/Al_2O_3 and $Au(Au_2O_3)$/ $Li_2O/CeO_2/Al_2O_3$. The EXAFS experimental spectra are given in Fig. 1. The extraction of EXAFS signal is based on the determination of the threshold energy for Au L_{III} edge followed by pre-edge and after-edge background removal with base line fitting with different modeling functions and by $\mu_0(k)$ and $\mu(k)$ evaluation with 3rd order bell spline functions. In according with Eq. (1) the EXAFS signals were performed in the range 37.5-140 nm^{-1}. In order to obtain the distribution of the atomic distances we calculated the radial structure function using Eq. (3) [1-2, 6]. The mean Au-Au distances of the first and the second coordination shell for standard sample, at room temperature have values close to R_1=0.287 and R_2=0.407 nm. Based on the Fourier transform of $k^3\chi(k)WF(k)$, performed in the range 0.02-0.5 nm, we obtained the magnitude of the atomic radial distribution $|\Phi(r)|$ for investigated samples as well as for standard Au foil. In order to avoid spurious errors due to limited interval in the wave vector space we have taken into consideration the Kaiser window function [7-8]. The Fourier transform magnitude is diminished as a result of the reduced average co-ordination number and the peaks in $|\Phi(r)|$ are shifted from the true distance due to the phase shift function that is included in the EXAFS signal. We proceeded by taking the inverse Fourier transform given by Eq (4) of the first neighboring peak and then extracting the amplitude function $A_j(k)$ and the phase shift function $\delta(k)$ in according with Eq. (2). By Lavenberg-Marquard fit of Eq. (2) and experimental contribution given by Eq.(4) for each coordination shell, we then evaluated the interatomic distances, number of neighbours and edge position. Table 1 contains the best values of the local structure parameters of the investigated samples and the errors given for the best-fit parameters, ΔN and ΔR. The average inter-atomic distances obtained for the first coordination shell have practically the same values as those of the standard sample. There was a difference of approximately 27% between the number of atoms of investigated catalysts and the standard sample (N_1=12). We considered that this diminution of the number of atoms is due to a strong electron interaction between the Au active metal and oxide supports [9-11].

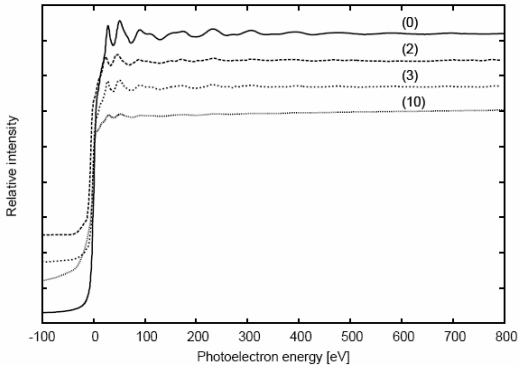

Fig. 1. The normalized absorption coefficients of Au L_{III} edge for the investigated samples.

Table 1. The local structural parameters of the investigated samples for the first coordination shell.

Sample	Atomic number $N_1 \pm \Delta N_1$	Shell radius [nm] $R_1 \pm \Delta R_1$
Au Foil	12	0.287
$Au/ZnO/MgO/Al_2O_3$	2.32±0.1	0.287±0.02
$Au/CuO/Al_2O_3$	4.61±0.13	0.287±0.01
$Au/Li_2O/CeO_2/Al_2O_3$	2.93±0.12	0.280±0.02

5.2. XRD results

Generally, it is not easy to obtain accurate values of the crystallite size and the microstrain parameter without extreme care in the experimental measurements and analysis of XRD data. The Fourier analysis of XRLP depends strongly on the magnitude and nature of the errors propagated in the data analysis. Three systematic errors are treated in papers [12-13]: uncorrected constant background, truncation and the effect of sampling for the observed profile at a finite number of points that appear in the discrete Fourier analysis. In order to minimize the propagation of these systematic errors, a global approximation of the XRLP is adopted instead of the discrete mathematical analysis. Therefore, in this paper, the structural parameters obtained from the diffraction line broadening in the X-ray powder pattern were analytically calculated using the GFF facilities. The reason for choosing this method, as described in Section 3, was the simplicity and the mathematical elegance of the analytical form of the Fourier transform magnitude and the integral width of the true XRLP given by Eqs.(7,9). This method was chosen against a numerical fast Fourier transform (FFT) whose validity depends on the filtering technique adopted [14]. In this way the accuracy of the global nanostructural parameters are closely related to the accuracy of the Fourier transform magnitude of the true XRLP.

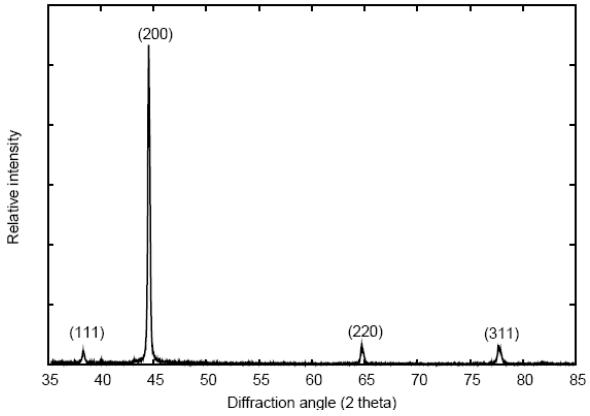

Fig. 2. The relative intensity of (111), (200), (220) and (311) experimental XRPL for Au foil as the instrumental function.

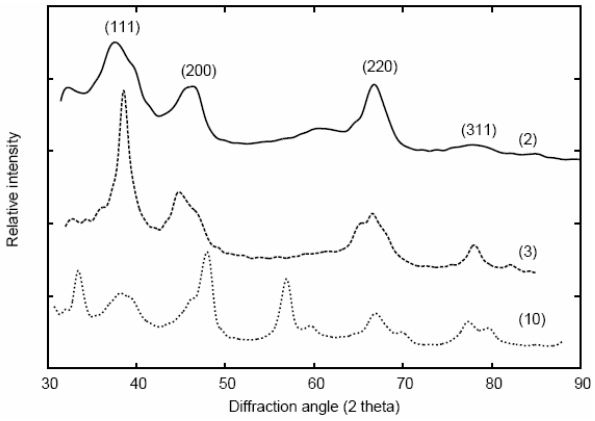

Fig. 3. The relative intensity of (111), (200), (220) and (311) experimental XRPL for (2), (3) and (10) supported gold catalysts samples.

The following profiles were processed: (111), (200), (220) and (311). Their experimental relative intensities with respect to the 2θ values and the Au foil spectrum as instrumental broadening effect are shown in Figs. 2-3. The background correction of the XRLP was done by polynomial procedures. The further steps in the analysis are the removal of the metallic oxides contribution from the XRLP, the doublet Rachinger correction [15] and the determination of the best parameters of the GFF distributions by nonlinear least squares fit. In order to determine the nanostructural parameters within Eq. (10) we computed the Fourier transforms of the true XRLP, and the integral width using Eqs. (7,9). In Section 4.2 we have shown that the coordination shells radii of the investigated samples have similar values as the Au foil. This important result is strongly correlated with the positions of (111), (200), (220) and (311) XRLP from the experimental spectra contained in Fig. 3. Therefore, these results explain the metal features of the bulk gold investigated clusters despite the strong deformation of the crystalline structure.

Carbon oxide chemisorption, transmission electron microscopy, magnetization, electronic paramagnetic resonance and other methods could have been used to determine the grain size of the particles by taking into account a prior spherical form for the grains. By XRD method one can obtain the crystallite size that has different values for different crystallographic planes. There is a large difference between the grain size and the crystallite size due to the physical meaning of the two concepts. It is possible that the grains of the gold are built up of many gold crystallites. The global structural parameters obtained for the investigated samples are summarized in Table II. The microstrain parameter of the lattice can also be correlated with the effective crystallite size in the following way: the value of the effective crystallite size increases when the microstrain value decreases. On the other hand, in many cases, the nano-crystallite size determined by Scherrer equation is greater than the one obtained by Eq. (10) because it does not take into account the lattice strains. Therefore, the crystallite size values determined by classical Scherrer equation [16] for nanostructured materials as supported metal catalysts are less reliable than the results obtained from Fourier transform method described in Section 3.

Table 2. The global structure parameters of the investigated samples.

Sample	XRLP	Crystallite size D_{eff} [nm]	Microstrain $\langle\varepsilon^2\rangle_{hkl}$ $\times 10^{-2}$
$Au/ZnO/MgO/Al_2O_3$	(111)	1.6	2.06
$Au/CuO/Al_2O_3$	(311)	5.8	0.40
$Au/Li_2O/CeO_2/Al_2O_3$	(311)	6.0	0.38

5.3. XPS results

The survey photoemission spectrum of $Au(Au_2O_3)/Li_2O/Ce_2O/Al_2O_3$ catalyst with the identification of the main XPS core level lines are presented in Fig. 4. Besides the spectral features related to the constituent elements of the supported gold catalysts only a weak C 1s peak has been detected. The presence of the C element is due to hydrocarbons absorbed on the surface of the sample powder. Along with the main lines there are loss peaks which are weaker and broader than the photoelectron peaks and appear in the spectrum as though they are at higher binding energy. Their appearance is due to the small crystallite sizes of the investigated samples.

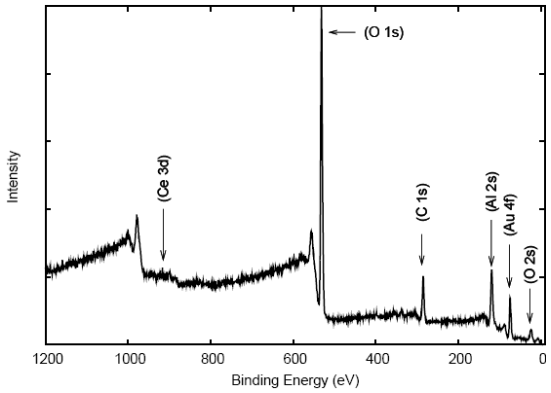

Fig. 4. XPS survey spectrum of the $Au(Au_2O_3)/Li_2O/CeO_2/Al_20_3$ sample.

In Fig. 5 is presented the O 1s line. It represents three contributions from oxide supports (Li_2O, CeO_2, Al_2O_3) and one that could be from Au oxide (Au_2O_3).

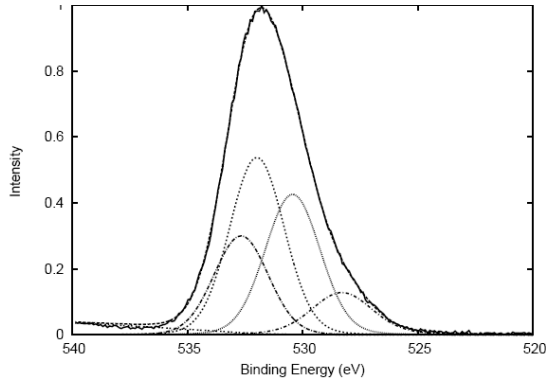

Fig. 5. XPS spectrum of O 1s lines for $Au(Au_2O_3)/Li_2O/CeO_2/Al_20_3$ sample.

Fig. 6 shows the contribution of the Ce 3d transitions containing six peaks. The peaks are spin-orbit split into a doublet, with each doublet showing further structure due to final state effects.

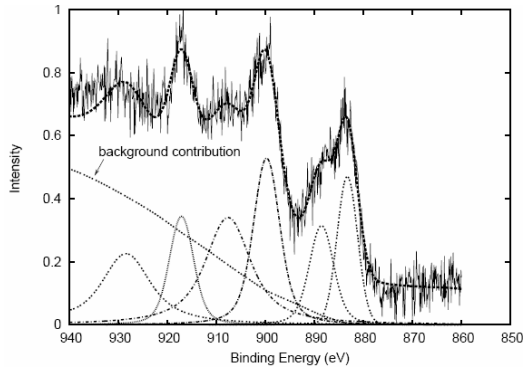

Fig. 6. XPS spectrum of Ce 3d lines for $Au(Au_2O_3)/Li_2O/CeO_2/Al_20_3$ sample.

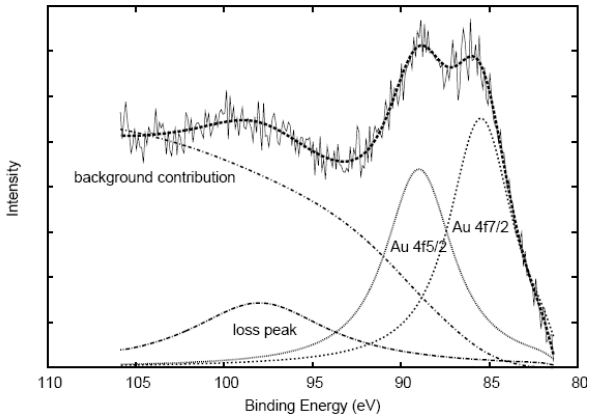

Fig. 7. XPS spectrum of Au 4f lines for $Au(Au_2O_3)/Li_2O/CeO_2/Al_20_3$ sample.

In Fig. 7 is shown the XPS spectrum in the Au 4f region of the active metal. It can be seen that the background strongly increases at high energy. If an emitted electron has two or more inelastic collisions, it contributes to the general background of a spectrum, so the background commonly increases to the high binding energy side of any major photoelectron peak. This region shows two peaks, due to the Au $4f_{7/2}$ and Au $4f_{5/2}$ transitions. The 4f line is spllited due to the spin orbit coupling. These peaks are centered at about 85.5 eV and 89 eV. The value 85.5 eV of the Au $4f_{7/2}$ is closely related to the 85.7 eV value, corresponding to Au oxide, than to Au in a metallic state (84 eV), which suggests that the gold is in an oxidized state. From previously information based on EXAFS and XRD measurements such as XRLP positions and the values of the first coordination shell, we evidenced only Au in a metal state. The oxidation state cannot be observed by EXAFS and XRD because these methods determine the crystalline structure in bulk gold crystallites while XPS gives information mainly from the surface of the investigated samples. This suggests that the Au oxidation state is present only on the surface of the crystallites [17-19].

6. Conclusions

In the present paper it has been shown that, in addition to EXAFS experiments with their specific advantages, XRD analysis can add more information for understanding bulk nanostructure of the gold nanoparticles and the XPS method gives us the electronic structure of gold nanoclusters and their multicomponents. The conclusions that can be drawn from these studies are:

(i) The diminution of the number of atoms from the first and the second coordination shells of Au in the investigated samples points out the existence of an electronic interaction between the gold nanoparticles and the oxide supports;

(ii) For XRLP analysis, a global approximation is applied rather than a numerical Fourier analysis. The

former analysis is better than a numerical calculation because it minimizes the systematic errors that can appear in the traditional Fourier analysis.

(iii) Our results showed that by using the GFF distribution we could successfully obtain reliable global nanostructural parameters.

(iv) The XPS method provided us additional information related to the possible existence of the gold oxide on the surface of the gold crystallites for the last investigated sample.

References

[1] N. Aldea, Andreea Gluhoi, P. Marginean, C. Cosma, Xie Yaning, Spectrochim. Acta Part B **55,** 997 (2000).

[2] N. Aldea, Andreea Gluhoi, P. Marginean, C. Cosma, Xie Yaning, Hu Tiandou, Whongua Wu and Baozhong Dong, Spectrochim. Acta B. Part B **57**, 1453 (2002).

[3] N. Aldea, B. Barz, T. D. Silipas, Florica Aldea Zhonghua Wu, J. Optoelectron. Adv. Mater. **7**(6), 3093 (2005).

[4] B. S. R. F. Activity Report 2003-2004, Beijing Electron Positron Collider National Laboratory.

[5] R Grisel, Kees-Jan Weststrate, Andrea Gluhoi, B. E. Nieuwenhuys, Gold Bulletin **35**(2), 45 (2002).

[6] F. W. Lytle, R. B. Greegor, E. C. Marques, D. R. Sandstrom, G. H. Via and J. H. Sinfelt, J. Catal. **95**, 548 (1985).

[7] San-Miguel, Physica B**208/209,** 177 (1995).

[8] N. Aldea, E. Indrea, Comput. Phys. Commun. **60**, 145 (1990).

[9] D. C. Koningsberger, B. C. Gates, Catal. Lett **14**, 271 (1992).

[10] C. H. Lin, S. H. Hsu, M.Y. Lee, S. D. Lin, J. Catal. **209**, 62,(2002).

[11] R. Zanella, S. Giorgio, C. H. Shin, C. R. Henry, C. Louis, J. Catal. **222**, 357 (2004).

[12] R. A. Young, R. J. Gerdes, A. J.Wilson, Acta Cryst. **22,** 155 (1967).

[13] N. Aldea, C. V. Tiusan, B. Barz, J. Optoelectron. Adv. Mater. **6**(1) 225 (2004).

[14] J. S. Walker, Fast Fourier Transform, Second Ed. CRC Boca Raton, New York, London, Tokyo, 1997.

[15] N. Aldea, E. Indrea, Comput Phys. Commun. **60**, 155 (1990).

[16] H. P. Kug, L. E. Alexander, X-ray diffraction procedures for polycrystalline and amorphous materials, 2nd ed. John Wiley and Sons, New York 1974.

[17] J. Guzman, B. C. Gates, J. Phys. Chem. **B 106**, 7659 (2002).

[18] J. Hua, K. Wei, Q. Zheng, X. Lin, Appl. Catal. **A 259**, 121 (2003).

[19] Z. Hao, A. Liduan, H. Wang, H.Tiandou, React. Kinet. Catal. Lett. **70,** 153 (2000).

*Corresponding author: naldea@s3.itim-cj.ro